Multi-Wavelength characterization of VVVX open clusters

C.O. Obasi[1]⋆, E. R. Garro[2], J.G. Fernández-Trincado[1]⋆⋆ , D. Minniti[3,4], M. Gómez[3], M. C. Parisi[5,6], and M. Ortigoza-Urdaneta[7]

[1] Instituto de Astronomía, Universidad Católica del Norte, Av. Angamos 0610, Antofagasta, Chile.

[2] ESO - European Southern Observatory, Alonso de Cordova 3107, Vitacura, Santiago, Chile

[3] Instituto de Astrofísica, Depto. de Ciencias Fisicas, Facultad de Ciencias Exactas, Universidad Andrés Bello, Av. Fernández Concha 700, Las Condes, Santiago, Chile

[4] Vatican Observatory, V00120 Vatican City State, Italy

[5] Observatorio Astronómico, Universidad Nacional de Córdoba, Laprida 854, X5000BGR Córdoba, Argentina

[6] Instituto de Astronomía Teórica y Experimental (CONICET-UNC), Laprida 854, X5000BGR Córdoba, Argentina

[7] Departamento de Matemática, Facultad de Ingeniería, Universidad de Atacama, Copiapó, Chile

ABSTRACT

Context. With the rise of large surveys across wavelengths, both supervised and unsupervised machine learning algorithms have increasingly aided in detecting large samples of old open clusters in high-extinction regions of the Milky Way bulge and disk.

Aims. Our primary goal is to confirm or discard automatically detected open clusters from poorly studied, heavily contaminated regions of the Milky Way. Cleaning these samples is critical for reconstructing the Galactic disk's star formation history and understanding the thin and thick disk formation model.

Methods. We used data from the VISTA Variables in the Via Láctea extended Survey (VVVX), Two Micron All-Sky Survey (2MASS), and *Gaia* Data Release 3 (*Gaia* DR3) to confirm and characterize nine open cluster candidates: BH118, BH 144, Schuster-MWSC 1756, Saurer 3, FSR 1521, Saurer 2, Haffner 10-FSR 1231, Juchert 12, and Pismis 3. We constructed density maps and vector-proper motion diagrams to analyse the targets. Additionally, we performed photometric analysis to derive their main physical parameters.

Results. We examined cluster images in 2MASS, Wide-field Infrared Survey Explorer (WISE), and Dark Energy Camera Plane Survey (DECaPS), identifying star clusters through an over-density of stars. This was confirmed with a VVVX photometry density map and validated using Gaussian Kernel Density Estimation. Using *Gaia* proper motion data, we refined cluster memberships and decontaminated the data to build the final cluster catalogue with high-likely star cluster members. We derived the following parameters: extinction values ranging from A_{K_s}=0.07±0.03 to 0.50±0.04 ; colour excess values from E(J-K$_s$)= 0.16±0.03 to 0.60±0.03 ; distances from D = 2.19±0.06 kpc to 8.94±0.06 kpc; Galactocentric distances from R$_G$= 7.82 kpc to 15.08 kpc; vertical distance component values from Z = -0.09 kpc to 0.34 kpc; and tangential velocities from V$_T$= 30.59 km/s to 245.42 km/s. We also computed age and metallicity by fitting Parsec isochrones, finding ages ranging from t= 20 Myr to 5 Gyr and metallicity from [Fe/H] = -0.5 to 0.5. Structural parameters include core radii from r$_c$ = 0.71' to 5.21', tidal radii from r$_t$ = 3.4' to 12.0', and concentration indices from c = 0.36 to 0.83.

Conclusions. we photometrically confirmed the open cluster nature for 9 targets in our compilation, updating their main physical parameters.

1. Introduction

In the last three decades, the interest in the studies of intermediate-age (ages between 100 Myr and 1 Gyr) and old Galactic Open Clusters (OCs; those older than 1 Gyr) have increased significantly (see e.g; Montgomery et al. 1994; Phelps 1994; Friel 1995; Tosi et al. 1998; Frinchaboy et al. 2004; Tosi et al. 2007; Friel et al. 2010; Angelo et al. 2019; Tarricq et al. 2022). The reason is that understanding their properties like ages, metallicities, and kinematics is fundamental to better discern the structure and formation history of the thin and thick disk (Carraro & Chiosi 1994).

In the era of extensive surveys, such as the Two Micron All-Sky Survey (2MASS) (Skrutskie et al. 2006) and *Gaia* (Gaia-Collaboration et al. 2016), there has been an explosion in the discovery of many new OCs. Kronberger et al. (2006) used Sloan Digital Sky Survey (SDSS; York et al. 2000) and 2MASS images of selected Milky Way regions to discover 66 stellar groupings. The morphologies, colour-magnitude diagrams, and stellar density distributions of these objects suggest they are potential OCs and none of them have previously been listed in any catalogue. In these studies, they provided extensive descriptions for 24 candidates considered the most likely OCs based on 2MASS photometry. Of these 24, only 9 objects had fundamental parameters determined by fitting the colour-magnitude diagrams with solar metallicity *Padova* isochrones (Marigo et al. 2017). An additional 10 cluster candidates had distance modulus and reddening derived from K$_s$ magnitudes and colour indices of helium-burning red clump stars.

The catalogue by Kharchenko et al. (2013) identified 3,006 real objects from an initial list of 3,784 targets obtained from various sources. While most of these objects are classified as OCs, the catalogue also includes stellar associations and globular clusters. It provides essential cluster parameters such as central position, apparent size, proper motion (PM), distance, colour excess, and age. However, 778 of the 3,006 objects were not confirmed.

In another study, Cantat-Gaudin et al. (2020) identified 2,000 clusters using *Gaia* DR2 astrometry. Using deep *Gaia* photometry down to G=18, they measured the distance, age, and reddening of these clusters. An artificial neural network, trained on pre-

⋆ Casmir Obasi: casmir.obasi@ucn.cl

⋆⋆ José G. Fernández-Trincado: jose.fernandez@ucn.cl

viously documented objects with well-defined parameters, was employed to estimate the parameters of these new clusters. Out of the 2,000 clusters analyzed, reliable parameters were obtained for 1,867.

The VVVX survey has played a central role in confirming many new globular and OCs within the Galactic bulge and central region, where spatial extinction is high (Saito et al. 2024; Obasi et al. 2023, 2024; Garro et al. 2022a,b, 2024). Recently, we utilized VVVX data to discover and characterize a new open cluster, Garro 3 (Garro et al. 2024).

Recent OC studies have also relied heavily on the *Gaia* survey for example, 628 OCs were discovered using the open cluster finder algorithm with *Gaia* EDR3 data by Castro-Ginard et al. (2022), and 704 new potential clusters were found with the sample-based clustering search method using *Gaia* EDR3 data by Hao et al. (2022). A machine-learning approach was developed using *Gaia*, with 23 new OCs in the Tycho- *Gaia* Astrometric Solution dataset (Castro-Ginard et al. 2018). Cantat-Gaudin et al. (2019) found 41 new OCs towards the Perseus Arm. Closer to this, Castro-Ginard et al. (2019) detected 53 new OCs towards the Galactic anti-center. These are just a few of the newly discovered OCs, with many more not mentioned here. However, many detected but unconfirmed clusters still lack characterization of their physical parameters.

Consequently, many new findings are considered potential OC candidates, and some are false positives when better observations are made. For example, FSR 1333, with J2000 coordinates α= 123.108, δ= -27.9130, and FSR 1651, with J2000 coordinates α= 201.382, δ= -58.9850, were both classified as open clusters by Buckner & Froebrich (2013). However, our current analysis using VVVX data revealed no over-density in the VVVX photometry density map and Gaussian Kernel density estimation (KDE), as shown in Figure 1. This suggests that both clusters might be false positive detections.

Therefore, it remains essential to confirm so many of these new detections and measure their physical parameters. In this context, one of the primary objectives of the VVV Team is to confirm new star clusters within the VVV, (Minniti et al. 2010; Saito et al. 2012) and its extension VVVX (Saito et al. 2024) based on observations at the VISTA 4m telescope. In this task, the importance of the VVV lies in its operating wavelength at the near-infrared (NIR), which has proved to be much more effective in the highly crowded central region of the Galactic bulge where high spatial extinction exists.

In this paper, we use a combination of VVVX, 2MASS, and optical *Gaia* DR3 (Gaia Collaboration et al. 2021) data listed in Table 1 to confirm and characterize the physical nature of nine selected OCs toward the Galactic bulge. Additionally, we provide the first physical measurements and characterization of Jurchert12. Section 2 describes the dataset sources used in this work. Section 3 outlines the methodology for the analysis. In Section 4, we present our derived physical parameters and a summary of the results. Section 5 presents the results, while Sections 6 and 7 present the discussion and conclusions.

2. Datasets

In this work, VVVX data in combination with 2MASS and *Gaia* DR3 was used to characterize nine OC candidates: BH118 , BH144, Schuster-MWSC1756, Saurer3, FSR1521, Saurer2, Haffner10-FSR1231, Juchert12 and Pismis3 listed in the catalogues of Kronberger et al. (2006); Kharchenko et al. (2013) and Cantat-Gaudin et al. (2020). These clusters had not been properly characterized before. Our datasets comprised both NIR and

optical data, and we used a matching radius of 0.5". The NIR data came from the VVVX and the 2MASS (Saito et al. 2024; Skrutskie et al. 2006). The VVVX is a public ESO survey, conducted with the VISTA Infrared Camera (VIRCAM) on the 4.1 m wide-field Visible and Infrared Survey Telescope for Astronomy (VISTA; Emerson & Sutherland 2010).

The point spread function (PSF) photometry was extracted as described by Alonso-García et al. (2018). Astrometry was calibrated to the *Gaia* Data Release 3 (DR3; Gaia Collaboration et al. 2021) reference system, while photometry was calibrated to the VISTA magnitude system (González-Fernández et al. 2018) against the 2MASS using a globally optimized model of frame-by-frame zero points plus an illumination correction. We used NIR 2MASS data to reach magnitudes brighter than Ks = 11, which are saturated in the VVVX images. Although we treated the VVVX and 2MASS data separately, we scaled them to the same photometric system (González-Fernández et al. 2018), applying correction offsets of ΔKs < 0.009 and ΔJ < 0.050 .

Previous studies on these clusters by Kronberger et al. (2006); Kharchenko et al. (2013), and Cantat-Gaudin et al. (2020) have produced conflicting results, with no generally agreed-upon properties. The inspection of the VVVX tiles that contain these clusters revealed a clear and well-separated over-density of red giant stars at their equatorial coordinates, listed in Table 1. This confirms their status as real star clusters. Additionally, we visually inspected all the cluster overdensities in the 2MASS, WISE, and DECaPS images to ensure that these features were not artefacts and remained consistent under small variations of parameters (i.e., observing the targets in different wavelengths).
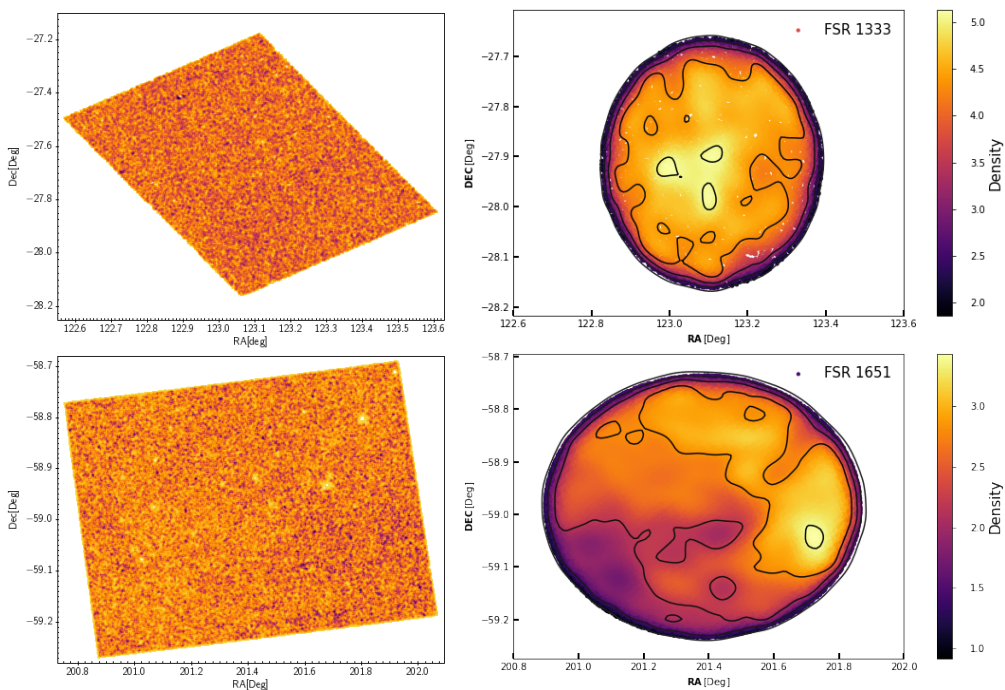
3. Methodology

To achieve the objectives of this study, we followed methods similar to those outlined in Obasi et al. (2021) and Garro et al. (2022b). We began our investigation by carefully examining images captured at various wavelengths, as shown in Figures 2 and A.4. Each figure contains four panels. The first and third panels display cluster images captured at various wavelengths. In all three images in the first and third panels, there is clear evidence of stellar overdensities, which resemble star clusters published in the literature. However, additional checks are required to validate our initial assumption since these overdensities are observed in a densely populated region.

First, we created a density map using VVVX photometry for the tiles corresponding to each cluster with the TOPCAT program (Taylor 2005), revealing a clear excess of stellar density at the cluster location, as shown in the left panels of Figures 2 and A.4 (second and fourth panels). Starting from the cluster locations in each tile, we applied cone selection and then performed KDE on the resulting data to examine the clusters' overdensities in more detail. This statistical method allows for a more accurate distinction between stellar overdensities and background fluctuations, beyond simple visual inspection. The KDE analysis confirmed a centralized, circular overdensity, as shown in the right panels of Figures 2 and A.4 (second and fourth panels). These tests provide compelling evidence that these objects are indeed star clusters.

3.1. Decontamination procedure and cluster membership

Studying the inner region of the Milky Way, such as the bulge and disk, is always challenging. Several factors contribute to

Fig. 1. VVVX density maps and Gaussian kernel density estimations for the clusters FSR 1333 and FSR 1651 are shown in the upper and lower panels left-right, respectively.
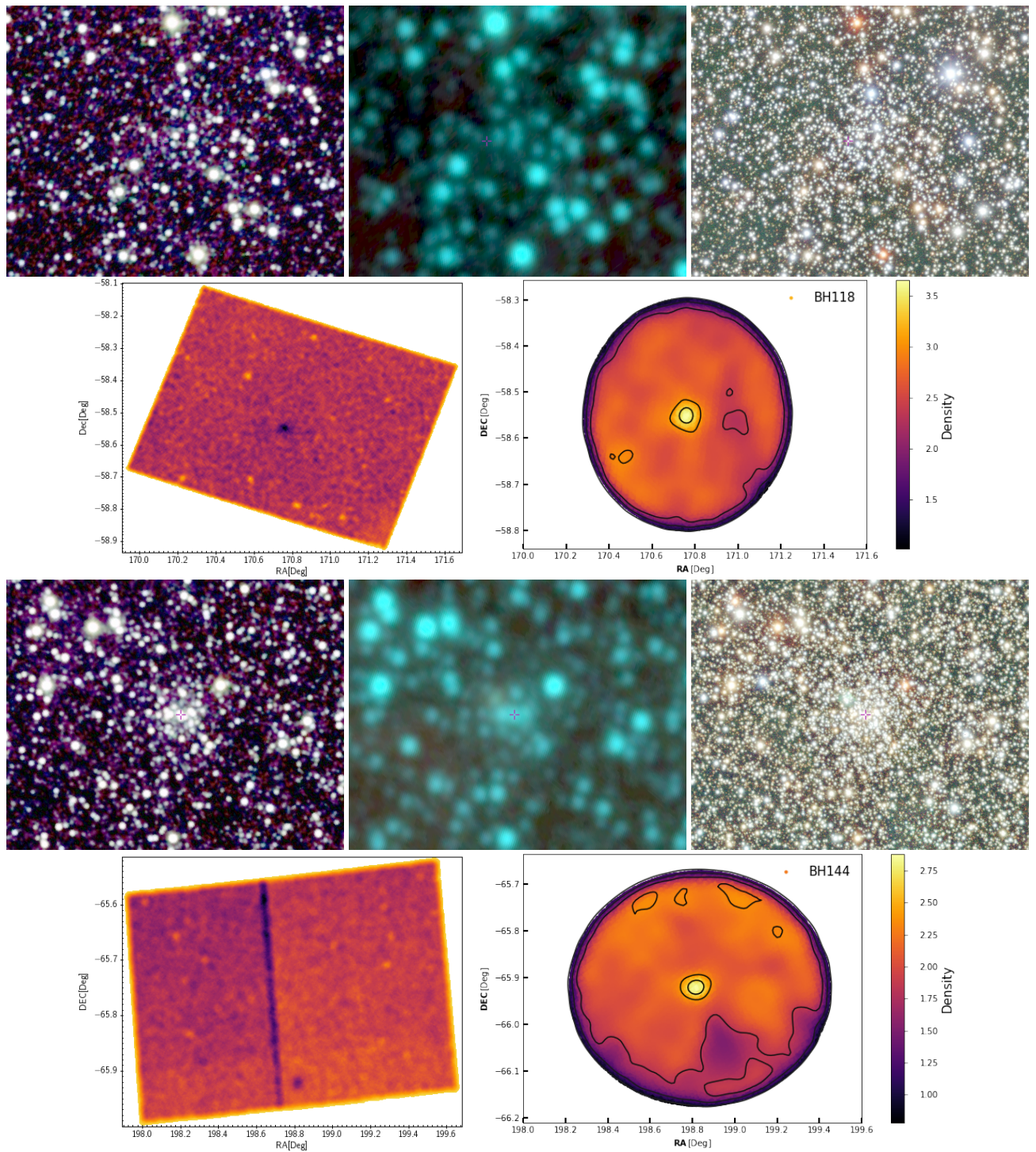
Table 1. Cluster name, coordinates (RA and Dec), Galactic coordinates (l and b), VVVX tile corresponding to each cluster, and literature references.

Name	Ra (h:m:s)	Dec (d:m:s)	l	b	VVVX-Tile Number	Ref
BH118	11:23:03.600	−58:32:56.40	291.6041	2.3655	e809	(a)
BH_144	13:15:20.424	−65:55:23.88	305.3625	−3.1619	e736-735	(b)
Schuster-MWSC1756	10:04:36.192	−55:51:24.84	281.0043	−0.2568	e1081	(b)
Saurer3	10:41:30.000	−55:18:00.00	285.1036	3.0091	e805	(b)
FSR1521	09:55:22.992	−56:36:05.76	280.4353	−1.6251	e1035	(b)
Saurer2	08:25:28.800	−39:37:48.00	257.9931	−0.9970	e1065	(b)
Haffner10-FSR1231	07:28:34.800	−15:21:54.00	230.7990	1.01100	e1091	(b)
Juchert12	07:20:56.712	−22:52:00.12	236.5614	−4.1232	e605	(c)
Pismis3	08:31:15.600	−38:39:28.80	257.8590	0.4803	e1110	(b)

References: (a) (Cantat-Gaudin et al. 2020), (b) (Kharchenko et al. 2013), (c) (Kronberger et al. 2006)

these difficulties, such as differential reddening and extinction. These factors not only impact the accuracy of photometric distance estimates but also influence derived cluster parameters such as age and metallicity. To mitigate some of these challenges, we applied the following cuts: $\pi < 0.5$" (parallax to avoid severe contamination from foreground stars) and renormalized unit weight error (ruwe) < 1.4 (a high-quality astrometric parameter). This ensures that all our photometric data have reliable astrometric solutions which is consistent with our previous studies (Garro et al. 2022b, 2024). We then used KDE iso-density contours (Figure 2 and A.4 second and fourth right panels) to statistically show the significance of the stellar overdensity and eliminate false positives masquerading as genuine stellar overdensities as we previously demonstrated in Figure 1. This method is also similar to our analysis in the previous paper (Garro et al. 2024). To refine our sample and eliminate contam-

inants, we computed the membership probability for each cluster. Accurate membership determination is crucial for deriving the clusters' astrophysical parameters. Vasilevskis et al. (1958) introduced the first mathematical model for membership determination, which was later refined by Sanders (1971) using the maximum likelihood principle. Since then, improved methods for determining star membership in clusters based on proper motions and different observed precisions have been developed (see Stetson 1980; Zhao & He 1990; Zhao & Shao 1994). We first applied a Gaussian Mixture Model (GMM) with two components to the PM data in RA and Dec to determine cluster membership probabilities, effectively separating cluster stars from field stars. For each group, we calculated the mean and standard deviations of $\mu_{\alpha*}$ and μ_δ. Furthermore, the separation of the two distributions (D) was quantified by comparing their means μ_1 and μ_2, normalized by their standard deviations σ_1 and σ_2. Using D, we

Fig. 2. Four panels are presented: The upper panel shows multi-band images of the open cluster BH118, with the left image from 2MASS, the middle from WISE, and the right from DECaPS. The second panel displays the cluster's density map on the left, highlighting the darkest region as the cluster location, and the KDE distribution on the right. The third and fourth panels present the same data for cluster BH144.

can measure how far apart the centres of two distributions are from each other. By doing this, we can determine whether the two distributions overlap or distinct. Our clusters have a minimum D value of 2.5, consistent with the threshold noted by Muratov & Gnedin (2010) and Ashman et al. (1994), who suggest that a clean separation between modes requires D>2. Figure 3 presents a histogram of the cluster and field distributions for

BH144, clearly illustrating the distinct separation of the cluster mean from the field.

We applied a straightforward yet effective method to estimate membership probabilities and identify probable cluster members based on proper motions, closely following the approach of Sanders (1971). We began by defining the proper motions (M_{xi}, M_{yi}) as well as their mean values (M_{xc}, M_{yc}), obtained by using the GMM code, along with their uncertainties $(E_{M_{xi}}, E_{M_{yi}})$.

σ_c represents the proper motion radius of the cluster. The normalized factor, (factor1), is defined as:

$$\text{factor1} = \sqrt{2\pi} \cdot \sqrt{\left(\sigma_c^2 + E_{M_{xi}}^2\right)\left(\sigma_c^2 + E_{M_{yi}}^2\right)} \tag{1}$$

Next, we calculated the squared distance between each star's proper motion and the cluster mean:

$$\begin{aligned} n_x^2 &= (M_{xi} - M_{xc})^2 \\ n_y^2 &= (M_{yi} - M_{yc})^2 \end{aligned} \tag{2}$$

The variances for pmra and pmdec are then defined as:

$$\begin{aligned} \sigma_{nx}^2 &= \sigma_c^2 + E_{M_{xi}}^2 \\ \sigma_{ny}^2 &= \sigma_c^2 + E_{M_{yi}}^2 \end{aligned} \tag{3}$$

We then computed the exponential component, known as factor2, for the membership probability:

$$\text{factor2} = \exp\left(-\frac{1}{2}\left(\frac{n_x^2}{\sigma_{nx}^2} + \frac{n_y^2}{\sigma_{ny}^2}\right)\right) \tag{4}$$

The unnormalized membership probability p_f is given by:

$$p_f = \frac{\text{factor2}}{\text{factor1}} \tag{5}$$

For clarity, we normalized the membership probabilities to a maximum of 1. This normalization allows for a clear distinction between cluster members and interlopers, defined by:

$$\text{pdf} = \frac{p_f}{\max(p_f)} \tag{6}$$

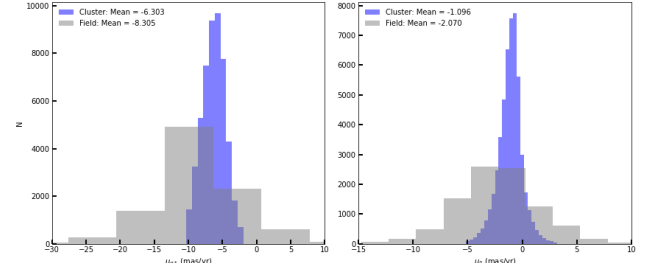We set our membership threshold T to classify stars as follows:

$$\text{Membership Status} = \begin{cases} \text{Member} & \text{if } p_f \geq T \\ \text{Non-Member} & \text{if } p_f < T \end{cases} \tag{7}$$

Our selection criteria were strict, with T typically set to ≥ 0.9 in most cases. Figure 4 shows the magnitude vs. membership probability plot for cluster BH144. The red dotted horizontal line indicates a 90% confidence level that a star belongs to the cluster.
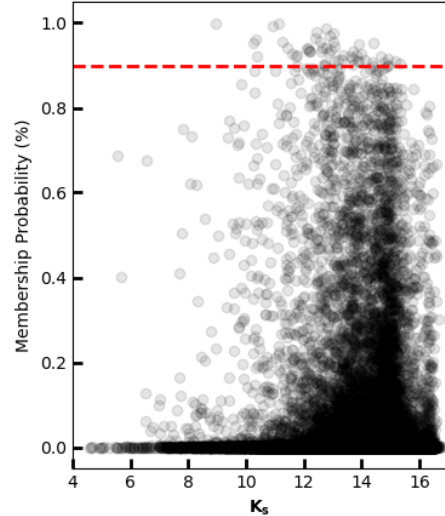
Subsequently, we constructed the colour-magnitude diagram (CMD) for all the clusters in both the 2MASS NIR and Optical *Gaia* data. In eight cases, distinct red clump (RC) stars are seen, as observed in Figure 5 for the cluster Pismis3. We measured the mean position of the RC overdensity using KDE to compute the max_density_index indicated by the dotted horizontal line and their corresponding error. For the clusters listed in Table 1, we present in Table 2 their K$_s$ and J-K$_s$ for the RC.

4. Estimation of the main physical parameters

We used the final catalogue obtained from our decontamination process for the rest of the analysis. We derived distance, reddening, and extinction. We built CMDs of the clusters and derived astrophysical parameters such as age and metallicity. The use of multiband photometry in our analysis, comprising VVVX+2MASS and Optical *Gaia*, helped us obtain more robust results. The structural parameters such as core radii, tidal radii and concentration parameters are presented in the next subsections.
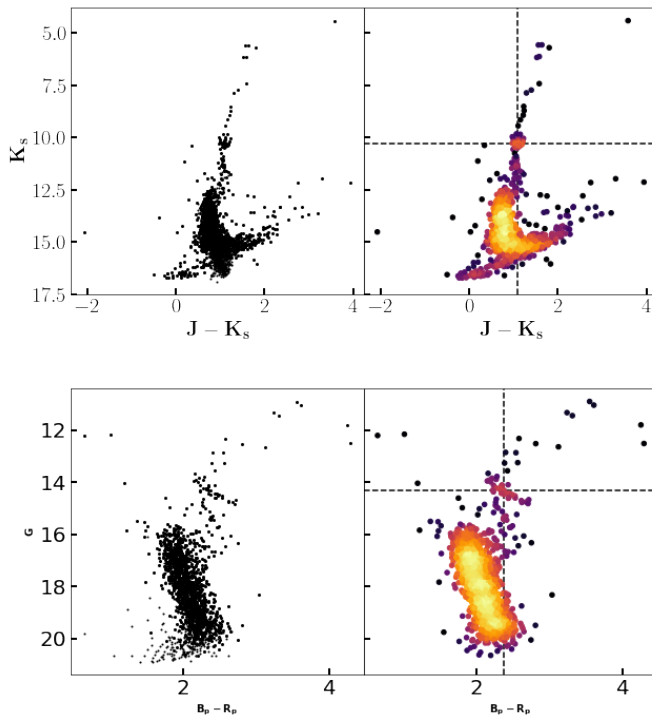

Fig. 3. The histograms of proper motions ($\mu_{\alpha*}$ and μ_{δ}), highlighting the distributions of the cluster (blue) and field (grey) populations along with their respective mean values.

Fig. 4. Membership probability as a function of K$_s$ magnitude is displayed, with a broken horizontal line indicating the 90% cluster membership threshold for BH144.

Table 2. Values of K_s and $J - K_s$ for the Red Clump

Name	K_s	$J - K_s$
BH118	13.082 ± 0.0145	0.818 ± 0.0163
BH_144	13.227 ± 0.039	0.831 ± 0.082
Schuster-MWSC1756	13.255 ± 0.029	2.0 ± 0.038
Saurer3	12.861 ± 0.025	1.031 ± 0.025
FSR1521	11.617 ± 0.015	2.10 ± 0.045
Saurer2	12.398±0.034	1.262 ± 0.015
Haffner10-FSR1231	−	−
Juchert12	13.275 ± 0.01	0.919 ± 0.263
Pismis3	10.303 ± 0.068	1.096 ± 0.079

Fig. 5. In the upper panel, we display the 2MASS NIR CMD (K_s vs. J-K_s). On the right, the RC overdensity is visible on the density map, and the horizontal line indicates the density peak. We present the same plot for optical *Gaia* data (G vs. BP-RP) in the bottom panel for Pismis3.

4.1. Reddening, extinction, distance, vertical component and tangential velocity

We computed the reddening and extinction associated with each cluster we studied. To do this, we followed the method outlined by Ruiz-Dern et al. (2018), as we have done in our previous studies (Obasi et al. 2021; Garro et al. 2022b). We used two methods to verify the position of the red clump stars in each cluster. First, we built the CMD (J vs. J-K_s) and used KDE to estimate the positions of K_s and J-K_s as demonstrated in Figure 5 (upper panel). We then verified the consistency of this method by constructing the generic luminosity function in the K_s band for each cluster, finding that the values obtained were in agreement.

Three methods were used to calibrate the extinction and reddening in our sample. First, we used Schlafly & Finkbeiner (2011) and Cardelli et al. (1989) to determine the extinction and reddening values. Second, we applied the extinction law from Nataf et al. (2015). Third, we calibrated our extinction and reddening values using the absolute magnitude of RC stars in the K_s band ($M_{K_s} = -1.605 \pm 0.009$) and their intrinsic colour ($(J - K_s)_0 = 0.66 \pm 0.02$) from (Ruiz-Dern et al. 2018). Based on these methods, we reported only the values from Nataf et al. (2015) and Ruiz-Dern et al. (2018), as they showed excellent agreement in their derived distances. We adopted the Ruiz-Dern et al. (2018) extinction law for the corrections. In Section 6, we will briefly discuss the reasons for the differences between these results and the exclusion of Schlafly & Finkbeiner (2011).

For the young cluster Haffner 10, whose CMD lacks a well-populated red RC sequence due to its age ($\sim$ 20 Myrs), we applied the extinction law derived by Nishiyama et al. (2009) (A_{K_s}=0.67· E(J - K_s)) to compute both extinction and reddening.

The derived extinction for all the clusters varied widely, ranging from A_{ks}= 0.07±0.03 to 0.50±0.04 , and the reddening ranged from E(J-Ks)$_0$= 0.16±0.03 to 0.60±0.03 . Using these values, we estimated the heliocentric distances of the clusters by applying the distance modulus equation. For Haffner 10, we first computed its distance using *Gaia* parallaxes. Both methods yielded similar distance results for each cluster; therefore, we adopted and reported the average values in table 4, which range from D = 2.19±0.06 kpc to D = 8.94±0.06 kpc.

We adopted $R_\odot$ = 8.2 kpc (Abuter et al. 2019) to compute the Galactocentric distance, which ranged from R_G= 7.82 kpc to 15.08 kpc. Using the relation Z = D×sin(b), assuming $Z_\odot$ = 0.007 kpc (Siegert 2019), we estimated the distance to the Galactic plane for each cluster, which ranged from Z= -0.09 kpc to 0.34 kpc, both below and above the Galactic plane. Finally, we computed the tangential velocities of each cluster, which ranged from V_T= 30.59 km/s to 245.42 km/s. This kinematic parameter allows us to deduce the Galactic component each of the clusters belongs to, which we will discuss further in the subsequent section.

4.2. Ages and Metallicities

Following a similar procedure to our previous work (Obasi et al. 2021) and taking into account our derived reddening values, extinctions, and distances for each cluster, we fitted PARSEC isochrones (Bressan et al. 2012). We visually inspected the fit until a match was obtained. Age and [Fe/H] were then obtained from this procedure.

We fixed the reddening and distance values estimated from the RC stars and fit the isochrones for different ages and metallicities. To derive robust fits, we varied the age and metallicity until an optimal match was found. This method reliably constrained the age and [Fe/H] for each cluster, as demonstrated in Section 6, where we discuss our results and compare them to values in the literature. The best-fitted isochrones in the VVVX and *Gaia* CMDs are shown in Figures 7 and A.5-A.8. The best-fitted parameters are listed in Table 4. The uncertainties in metallicities and distances in our study are estimated to be approximately 0.5 dex in ages and 0.2 dex in metallicities, consistent with findings from similar studies on open clusters (e.g.; Garro et al. 2024; Saroon et al. 2024).

4.3. Structural parameters

We measured the physical size of the clusters following a similar approach used by Obasi et al. (2021). First, we computed the Radial Density Profile (RDP). The initial centre coordinates obtained from the literature for each cluster were recomputed. The new centre was determined by calculating the median values of μ_α and μ_δ within a radius of 0.1' from the literature values. This newly derived centre was then used to build the RDPs.

For each cluster, we divided our sample into circular annuli with increasing radii moving outward from the centre. The number density per bin was computed as the number of stars (N) in the bin divided by the area (A). The RDP profile for each cluster is plotted as a function of the mean distance of the circular annulus from the cluster centre against the number density in the corresponding annuli. The error bars were computed as $e = \sqrt{N/A}$, following the method used in our previous work (Garro et al. 2022b). We subtracted the background level, which varies from 0.3 to 0.8 stars/arcmin^2, depending on the cluster.

To derive the physical parameters of the clusters, we used the model by King (1962) to fit the cluster density profile. From the best-fit parameters, we obtained the core radius (r_c), which ranges from 0.71' to 5.21'; the tidal radius (r_t), varying from 3.6' to 12'; and the concentration parameter (c), which ranges from 0.36' to 0.83'. See Figure A.9 for details.

5. Results

We employed a multiwavelength approach using VVVX+ *Gaia* DR3 and 2MASS+ *Gaia* DR3 to improve measurements, resolve inconsistencies from previous literature, and provide a detailed characterization of Jurchert12 for the first time. This study encompasses nine open clusters.

We began by deriving the extinction and reddening values for each cluster using the relation provided by Nataf et al. (2015), where A_V/A_{K_s} = 13.44 and E(J-Ks)/A_{K_s} = 0.43. This relation is optimized for the Milky Way's inner region, where extinction levels are particularly high. The results obtained from this method were compared with those from Ruiz-Dern et al. (2018) to ensure consistency. The A_V values for each cluster were retrieved from the NASA/IPAC database[1], which uses the relation from Schlafly & Finkbeiner (2011) to compute A_V.

For BH118, we found A_V = 1.66 ± 0.10 and E(B-V) = 0.53 ± 0.05 . For BH144, we found A_V = 2.52 ± 0.10 and E(B-V) = 0.81 ± 0.06 . The results for the other clusters are presented in Table 3 and 4.

Next, we applied the extinction and reddening relation by Nataf et al. (2015) to determine each cluster's NIR extinction and reddening. For BH118, we obtained A_{K_s} = 0.12 ± 0.01 and E(J-K$_s$) = 0.05 ± 0.0. For BH144, we found A_{K_s} = 0.19 ± 0.01 and E(J-K$_s$) = 0.08 ± 0.0. The values for the other clusters are presented in table 3.

Using these parameters and the absolute M_K derived by Alves et al. (2002) M_K=-1.61±0.03, we estimated the distance modulus $(m − M)_0$ for each cluster: 14.57 ± 0.03 for BH118, 14.65 ± 0.05 for BH144. We have reported the results for other clusters in table 3.
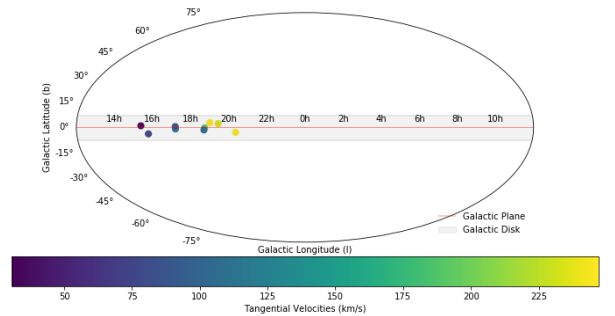
These values translate to heliocentric distances of 8.20 ± 0.13 kpc for BH118, 8.53 ± 0.20 kpc for BH144. The results for other clusters are presented in table 3.

We then validated these values using the Ruiz-Dern et al. (2018) relation. After measuring the RC positions in each cluster. To compute for the extinction we adopted the relation given in Alonso-García et al. (2017) (A_{K_s}/(E(J-K$_s$)=0.428±0.005) we found the following NIR extinction and excess colour values: for BH118, A_{K_s} = 0.07 ± 0.03 and E(J − K$_s$) = 0.16 ± 0.03; for BH144, A_{K_s} = 0.07 ± 0.08 and E(J − K$_s$) = 0.17 ± 0.08. We have presented the results for the other clusters in table 3. These values were used to estimate the distance modulus and distances to the clusters, resulting in the following: for BH118, 14.61 ± 0.03 and 8.36 ± 0.03 kpc; for BH144, 14.76 ± 0.11 and 8.95 ± 0.11 kpc. The other cluster's results are listed in table 3.

Although extinction and reddening were calculated differently using the methods from Nataf et al. (2015) and Ruiz-Dern et al. (2018), both approaches yielded distance results in excellent agreement . We averaged the distances from these methods (see Table 4) and compared them with those obtained using *Gaia* data. For *Gaia*, we used the Babusiaux et al. (2018) relation to compute extinction A_G and colour excess Bp-Rp. Since higher extinction affects distance calculations, we only reported

---

[1] https://irsa.ipac.caltech.edu/cgi-bin/bgTools/nph-bgExec

distances for clusters with A_G < 4 . The *Gaia* distances and the A_G value from the *Gaia* data are presented in Table 4, and the *Gaia* distances are within 2σ of the other distances. Furthermore, we used the new average distances to calculate the Galactocentric distance R_G for each cluster, adopting $R_\odot$ = 8.2 kpc (Abuter et al. 2019). The R_G values obtained ranged from 7.82 kpc to 15.08 kpc (see Table 4 for details). Furthermore, we computed the vertical distance Z, which ranged from -0.09 to 0.34 kpc for all clusters. Figure 6 shows the sky distribution of the clusters according to vertical distance (see Table 4 for the complete Z values). In Table 4, the computed proper motion and tangential velocities for each cluster are also shown.

Finally, using isochrone fitting, we estimated the ages and [Fe/H] values for all clusters. The ages range from 20 Myrs to 5 Gyrs, while the [Fe/H] values range from -0.5 to 0.5 dex. The results of the isochrone fitting are presented in Table 4. Additionally, we derived structural parameters for the clusters, including core radius (r_c), tidal radius (r_t), and concentration index (c). The structural parameter values, also shown in Table 4, confirm that all the clusters are genuine open clusters and none have undergone core collapse.

Fig. 6. A sky distribution plot of all nine clusters, showing their positions in Galactic coordinates (longitude *l* and latitude *b*, with colour representing their tangential velocities.

6. Discussion

A discussion of our results is presented in this section, along with a comparison of our obtained values with those found in the literature where available. In order to improve previous measurements and study the cluster in detail, we used a multiwavelength approach using VVVX+*Gaia* DR3 and 2MASS+*Gaia* DR3. This discussion begins by comparing each object with literature values, followed by an observation of the general trends observed across the sample.

BH118: For the cluster BH118, we obtained A_V = 1.66 ± 0.10 and E(B-V) = 0.53 ± 0.05. Cantat-Gaudin et al. (2020), however, reported a lower extinction value of A_V = 1.07. Using both Nataf methods and the Ruiz-Dern method for NIR, we obtained the following values: A_{K_s} and E(J-K$_s$) as 0.12 ± 0.01, 0.05 ± 0.003 and 0.07 ± 0.03, 0.16 ± 0.03, respectively. With these parameters, we computed a distance modulus of 14.57 ± 0.03 and 14.61 ± 0.03, equivalent to distances of 8.20 ± 0.13 kpc and 8.36 ± 0.03 kpc for both methods. Both results are in good agreement with those obtained by Cantat-Gaudin et al. (2020), where (m-M)$_0$ = 14.72 and D = 8.8 kpc. The Galactocentric distance R_G of 9.20 kpc we computed for BH118 is consistent with

Table 3. Extinction, reddening, distance modulus, and distances for the clusters.

Nataf method						
Name	A_V	E(B-V)	A_{K_s}	E(J-K_s)	$(m-M)_0$	D (kpc)
BH118	1.66±0.10	0.53±0.05	0.12±0.01	0.05±0.00	14.57±0.02	8.18±0.07
BH144	2.52±0.10	0.81±0.06	0.19±0.01	0.08±0.00	14.64±0.04	8.51±0.16
Schuster-MWSC1756	10.76±0.10	3.47±0.20	0.80±0.01	0.34±0.01	14.06±0.03	6.49±0.10
Saurer3	2.56±0.10	0.83±0.06	0.19±0.01	0.08±0.00	14.28±0.03	7.16±0.09
FSR1521	10.32±0.10	3.33±0.20	0.77±0.01	0.33±0.01	12.45±0.02	3.09±0.03
Saurer2	5.85±0.10	1.89±0.11	0.43±0.01	0.19±0.04	13.56±0.04	5.14±0.09
Haffner10-FSR1231	2.05±0.10	0.66±0.05	0.15±0.01	0.07±0.00	12.66±0.04	3.62±0.07
Jurchert12	2.60±0.10	0.84±0.06	0.19±0.01	0.08±0.00	14.69±0.02	8.84±0.07
Pismis3	4.37±0.10	1.41±0.09	0.33±0.09	0.14±0.04	11.72±0.07	2.20±0.07
Ruiz-Dern method						
BH118			0.07±0.03	0.16±0.03	14.61±0.03	8.36±0.03
BH144			0.07±0.08	0.17±0.08	14.76±0.11	8.95±0.11
Schuster-MWSC1756			0.57±0.04	1.34±0.04	14.29±0.05	7.21±0.05
Saurer3			0.16±0.03	0.37±0.03	14.30±0.04	7.25±0.04
FSR1521			0.62±0.05	1.44±0.05	12.59±0.10	3.31±0.10
Saurer2			0.26±0.03	0.60±0.03	13.74±0.05	5.59±0.05
Haffner10-FSR1231	–	–	–	–	–	–
Jurchert12			0.11±0.07	0.26±0.07	14.77±0.07	8.97±0.07
Pismis3			0.19±0.08	0.44±0.08	11.71±0.10	2.19±0.10

Note: The Nataf method derives from the relation presented in Nataf et al. (2015). However, we obtained the A_V values from the NASA/IPAC Infrared Science Archive (`https://irsa.ipac.caltech.edu/applications/DUST/`), which uses the extinction maps from Schlafly & Finkbeiner (2011) and Schlegel et al. (1998) to compute A_V for a given source. For our analysis, we adopted the values provided by SF11. It is important to note that the errors in A_{K_s} and E(J-K_s) are not zero. When rounded to three decimal places, the values are A_{K_s} = *[0.008,0.008,0.013,0.008,0.013,0.010,0.010,0.086]* and E(J-K_s) = *[0.003,0.003,0.006,0.003,0.006,0.041,0.003,0.003,0.037].*

the 9.6 kpc value obtained by Cantat-Gaudin et al. (2020). Additionally, the vertical distance of 0.34 kpc we obtained aligns with the 0.36 kpc reported by Cantat-Gaudin et al. (2020).

Our computed proper motion values μ_α = -5.821 ± 0.209 mas yr^{-1} and μ_δ = 1.609 ± 0.280 mas yr^{-1} are in good agreement with those computed by Cantat-Gaudin et al. (2020), which are μ_α = -4.406 mas yr^{-1} and μ_δ = 1.450 mas yr^{-1}. Furthermore, we derived the tangential velocities using these proper motions and distances as $V_{T\alpha*}$ ≈ -225.42 km/s and $V_{T\delta}$ ≈ 62.31 km/s. These positional and kinematic parameters suggest that BH118 is a disk cluster, as we will discuss later in this section. Finally, we derived an age of 3 ± 0.5 Gyr and [Fe/H] = -0.5 dex . However, Cantat-Gaudin et al. (2020) estimated the age of BH118 to be ≈ 2 Gyr. We over-plotted the isochrone family of 5, 3, and 2 Gyr to the CMD, as shown in Figure 7. The 3 Gyr isochrone provides a much better fit to the cluster. The core radius (r_c), tidal radius (r_t), and concentration index (c) of 0.86 ± 0.08', 5.76 ± 0.92' (see Figure A.9), and 0.83, respectively, all indicate a typical open cluster found in the disk (see Garro et al. 2022b; Saroon et al. 2024).

BH144: For BH144, our derived A_V value of 2.52 ± 0.10 is slightly higher than the value provided by Cantat-Gaudin et al. (2020) A_V = 1.68 . However, our colour excess E(B-V) = 0.81 ± 0.06 is in good agreement with the value of 0.63 obtained by Kharchenko et al. (2013). Using the two methods previously described, we obtained A_{Ks} and E(J-K_s) values of 0.19 ± 0.01 , 0.08 ± 0.0 and 0.07 ± 0.08 , 0.17 ± 0.08 , respectively. The distance we computed using the Ruiz-Dern method, 8.95 kpc, agrees with the Cantat-Gaudin et al. (2020) estimation of 9.6 kpc. Furthermore, our computed Galactocentric distance R_G = 7.82 kpc aligns with the value calculated by Cantat-Gaudin et al.

(2020) of 8.3 kpc. Our calculated vertical distance of -0.49 kpc also agrees with the value of -0.53 kpc reported by Cantat-Gaudin et al. (2020). Our proper motion values are in excellent agreement with those of Cantat-Gaudin et al. (2020) (see Table 4 for comparison). However, the values computed by Kharchenko et al. (2013) μ_α = -13.19 mas yr^{-1} and μ_δ = 7.74 mas yr^{-1} largely deviate from our calculations. Similarly, the values provided by Dias et al. (2014) μ_α = -4.73 mas yr^{-1} and μ_δ = -3.36 mas yr^{-1} also deviate slightly from our values. Our derived tangential velocities for BH144 (see Table 4) suggest that this cluster is located in the disk. Finally, isochrones of 6, 4, and 2 Gyr were utilized, with the best fit at 2 ± 0.2 Gyr and [Fe/H] = 0.5 dex. Kharchenko et al. (2013) estimated an age of 1 Gyr with [Fe/H] = -0.5 dex, while Cantat-Gaudin et al. (2020) derived an age of 1.5 Gyr, consistent with our findings (see Figure A.5). The structural parameters r_c and r_t of 1.9 pc and 11.88 pc slightly differ from Kharchenko et al. (2013) values of 0.83 pc and 12.88 pc.

Schuster-MWSC1756: We calculated A_V = 10.76 ± 0.10 and E(B-V) = 3.47 ± 0.20 for the cluster Schuster-MWSC1756. In contrast, Kharchenko et al. (2013) calculated a lower colour excess of E(B-V) = 1.08 . In Table 3, we report our NIR A_{K_s}, E(J-K_s) values, the distance modulus, and cluster distance, while in Table 4 we report the Galactocentric distance based on these parameters.

Our computed proper motion values are in good agreement with those computed by Cantat-Gaudin et al. (2020) (see Table 4), but they differ significantly from the values obtained by Kharchenko et al. (2013) μ_α = -9.41 mas yr^{-1} and μ_δ = 3.06 mas yr^{-1}. The tangential velocities suggest that this cluster lies in the disk. Of all the clusters we examined, Schuster-MWSC175

is the smallest size, with core and tidal radii of r_c = 1.4 pc and r_t = 7.04 pc, respectively (See Figure A.9). Given the high extinction in this cluster (A_V > 10), effective decontamination was challenging, particularly in the *Gaia* optical CMD. We compared isochrone fits at 400, 700, and 900 Myr with [Fe/H] of -0.5,0.0 and 0.0 dex (see Figure A.6); however, the sparsity of the CMD data makes it difficult to precisely determine the cluster's age, which tends to be at 700 Myrs. Nevertheless, it appears significantly older than the 6.3 Myr estimated by Kharchenko et al. (2013). For clusters with $A_V \geq 5$, we did not derive distances using Gaia data, and therefore we did not fit any isochrones on them.

Saurer 3: The E(B-V) = 0.83 ± 0.06 value we obtained for Saurer 3 is consistent with the 0.78 derived by Kharchenko et al. (2013). However, our computed proper motion values, μ_α = -6.62 ± 0.20 mas yr^{-1} and μ_δ = 3.24 ± 0.91 mas yr^{-1}, differ from those computed by Dias et al. (2014), who estimated μ_α = -6.73 mas yr^{-1} and μ_δ = -1.62 mas yr^{-1}. These values are also significantly different from those obtained by Kharchenko et al. (2013), which are μ_α = -8.34 mas yr^{-1} and μ_δ = 4.40 mas yr^{-1}. Furthermore, our derived age of 2 ± 0.2 Gyr and [Fe/H] = 0.5 dex (See Figure A.6 bottom panel) aligns closely with the $\approx$ 2 Gyr estimate reported by Kharchenko et al. (2013). We also derived structural parameters: a r_c of 0.79 ± 0.12' (corresponding to (r_c = 1.6) pc), a r_t of 4.65 ± 0.21' (corresponding to (r_t = 9.6 pc), and a concentration index (c) of 0.77. These values are significantly different from those provided by (Kharchenko et al. 2013), which are r_c = 9.18 pc and r_t = 20.46 pc, respectively.

FSR 1521: Cantat-Gaudin et al. (2020) obtained an A_V of 2.72, which is about eight magnitudes smaller than the A_V=10.32 ± 0.10 that we obtained for the cluster FSR 1521 using the extinction relation from Schlafly & Finkbeiner (2011). Additionally, our E(B-V) = 3.33 ± 0.20 differs significantly from the 0.37 measured by Kharchenko et al. (2013). These differences between our values and those in the literature might stem from our approach to computing optical extinction, where we use values provided by Schlafly & Finkbeiner (2011).

Our computed (m - M)$_0$ = 12.46 ± 0.03 and distance of 3.10 ± 0.05 kpc agree reasonably well with (m - M)$_0$ = 13.47 and D = 4.9 kpc reported by Cantat-Gaudin et al. (2020). We computed a Galactocentric distance R_G = 8.23 kpc, which is consistent with the 8.8 kpc calculated by Cantat-Gaudin et al. (2020). Similarly, our vertical-horizontal distance is consistent with the value provided by Cantat-Gaudin et al. (2020) (see Table 4 for comparison). Our proper motion value is also in agreement with those obtained by Cantat-Gaudin et al. (2020) (see Table 4 for comparison). However, the value -8.92 mas yr^{-1}, 6.10 mas yr^{-1} provided by Kharchenko et al. (2013) significantly differs from our computed value.

Using isochrone fitting, we estimated the cluster's age to be 1 ± 0.2 Gyr and [Fe/H] = 0.0 dex, as shown in the upper panel of Figure A.7. This age estimate differs significantly from previous studies: Cantat-Gaudin et al. (2020) reported an age of 5.2 Gyr, which appears to be an overestimate, while Kharchenko et al. (2013) calculated an age of 5 Myr, likely underestimating the cluster's age. We also derived structural parameters: a r_c of 2.19 ± 0.27' (corresponding to r_c = 2.5 pc), a r_t of 7.69 ± 0.92' (corresponding to r_t = 8.9 pc), and a concentration index c of 0.55. However, our measured values significantly differ from those obtained by Kharchenko et al. (2013), who reported r_c = 0.84 pc and r_t = 6.69 pc, respectively.

Saurer 2: We obtained A_V = 5.85 ± 0.10 for the cluster Saurer 2. This value contrasts with the A_V = 3.72 derived by Cantat-Gaudin et al. (2020), while our colour excess E(B-V) =

1.89 ± 0.11 is consistent with the 1.25 derived by Kharchenko et al. (2013). Our computed distance of 5.15 ± 0.11 kpc is in good agreement with the value of D = 6.4 kpc obtained by Cantat-Gaudin et al. (2020). Furthermore, our computed Galactocentric distance R_G = 10.77 kpc also aligns well with the R_G = 12.1 kpc obtained by Cantat-Gaudin et al. (2020).

Our measured Saurer 2 vertical-horizontal distance of -0.10 kpc is consistent with the -0.13 kpc value computed by Cantat-Gaudin et al. (2020). In the same way, our computed proper motion agrees well with that of Cantat-Gaudin et al. (2020) (see Table 4 for comparison), but it differs significantly from the values reported by Kharchenko et al. (2013) (see also Table 4). Using isochrone fitting, we estimated the cluster's age to be 700 ± 0.2 Myr with [Fe/H] = 0.5 dex (See Figure A.6 upper left panel). This estimate contrasts with the ages of 1.6 Gyr and 1.8 Gyr reported by Cantat-Gaudin et al. (2020) and Kharchenko et al. (2013), respectively, both of which likely overestimate the cluster's age. The structural parameters derived for Saurer 2 r_c = 1.4 pc, r_t = 7.8 pc (See Figure A.9) are in good agreement with those measured by Kharchenko et al. (2013) r_c = 1.4 pc and r_t = 15.56 pc.

Haffner10-FSR1231: There are a few parameters available for comparison with Haffner 10. However, the distance of 3.4 kpc computed by Cantat-Gaudin et al. (2020) is in good agreement with the 3.63 ± 0.09 kpc we obtained. The proper motion we computed is also in good agreement with those provided by Cantat-Gaudin et al. (2020) and Dias et al. (2014) (see Table 4 for comparison). We estimated an age of 20 ± 0.2 Myr and [Fe/H] = 0.5 dex for the cluster Haffner 10, which is notably different from the 3.8 Gyr age reported by Cantat-Gaudin et al. (2020). Our result indicates that Haffner 10 is a much younger open cluster than previously thought. (see Figure A.7 bottom panel). The other parameters derived for this cluster are listed in Tables 3 and 4.

Juchert 12: Juchert 12 is an open cluster catalogued by Kronberger et al. (2006). Its J2000 coordinates are μ_α = 07:20:56.712 and μ_δ = -22:52:00.12, with Galactic coordinates l = 236.5614 and b = -4.1232. To the best of our knowledge, this cluster has not been previously characterized. The only parameter available in the literature is the proper motion value estimated by Dias et al. (2014), who reported μ_α = -3.46 mas yr^{-1} and μ_δ = 0.52 mas yr^{-1}. These values contrast with our findings, which are μ_α = -0.75 ± 0.026 mas yr^{-1} and μ_δ = 1.62 ± 0.051 mas yr^{-1}. In this analysis, we determined the physical parameters of this cluster for the first time. Through isochrone fitting, we estimated an age of 2 Gyr and an [Fe/H]=0.5 dex (See Figure A.8 upper panel). Additional parameters for this cluster are presented in Tables 3 and 4.

Pismis 3: The A_V = 2.35 obtained by Cantat-Gaudin et al. (2020) is lower than the 4.37 ± 0.10 we derived from our analysis. We computed a distance of 2.19 ± 0.06 kpc for the cluster, which agrees with the 2.35 kpc estimated by Cantat-Gaudin et al. (2020). Additionally, our computed proper motion values μ_α = -4.76 ± 0.38 mas yr^{-1} and μ_δ = 6.66 ± 0.01 mas yr^{-1} agree with those provided by Cantat-Gaudin et al. (2020) (see Table 4 for comparison). However, these values slightly differ from those computed by Dias et al. (2014) μ_α = -3.42 mas yr^{-1} and μ_δ = 3.82 mas yr^{-1}). Furthermore, we estimated an age of 3 ± 0.2 Gyr and [Fe/H] = 0.5 dex for Pismis 3 (See Figure A.8 bottom panel), which is in excellent agreement with the 3 Gyr computed by Cantat-Gaudin et al. (2020). The other physical parameters, such as tangential velocities, vertical-horizontal distance, and core and tidal radius, whose values are consistent with those

expected for open clusters, are computed for the cluster and reported in Table 4.

In Figure 6, we present a sky distribution plot of all the clusters, showing their positions in Galactic coordinates *l* and *b*, with the colour representing their tangential velocities (V_T). The Galactic plane is indicated by the red line at *b* = 0°, and the Galactic disk is shown as the shaded area. We observed that the clusters are mostly concentrated near the Galactic plane *b* ≈ 0°, suggesting that they are part of or close to the Galactic disk, a characteristic observed in other open clusters. This concentration near the Galactic plane indicates that these clusters likely belong to the Milky Way disk. By the comparison, we can conclude that

a.) While our derived values closely agree with those provided by Cantat-Gaudin et al. (2020), they differ from those provided by Kharchenko et al. (2013) and Dias et al. (2014). b.) Unlike in other studies, which study these clusters as a group, we examined each individually in detail in this present analysis. c.) Eight of the examined clusters have their [Fe/H] values roughly estimated for the first time.

d.) We provided a detailed characterization of the clusters Juchert 12 and Haffner 10 for the first time.

Finally, in this study, we applied three extinction laws: Schlafly & Finkbeiner (2011),Nataf et al. (2015) and Ruiz-Dern et al. (2018). After comparing the results, we adopted and reported results from the two methods that showed the highest agreement. Here are our findings: The distances derived using the Ruiz-Dern et al. (2018) and Nataf et al. (2015) extinction laws demonstrated the highest level of agreement, with absolute differences typically within 0.5 kpc. This similarity likely arises from their shared reliance on robust extinction correction methods. Ruiz-Dern's method integrates precise *Gaia*-based parameters, while Nataf employs advanced bulge calibration techniques. These similarities make both approaches highly suitable for analyzing star clusters in regions with high extinction variations, especially near the Galactic bulge. In contrast, distances calculated using the SF11 extinction law consistently deviated, with differences exceeding 1.0 kpc for clusters such as Schuster-MWSC1756 (*b* = -0.2568), FSR1521 (*b* = -1.6251), and Saurer 2 (*b* = -0.9970). These clusters are located in low Galactic latitudes, where extinction is particularly severe. The SF11 method relies on two-dimensional dust maps, which tend to overestimate extinction in dense, heavily reddened regions. As Nataf et al. (2015) pointed out, these maps are less effective at resolving extinction variations in high-density areas, limiting their accuracy for clusters like those examined in this study.

7. Conclusions

We have provided updated measurements for the nine open clusters we studied and, for the first time, a detailed characterization of the cluster Juchert 12. Our derived parameters, where available, agree with those provided by (Cantat-Gaudin et al. 2020). However, our results conflict with those provided by Kharchenko et al. (2013) and Dias et al. (2014). The colour-magnitude diagrams, ages, metallicities, structural parameters, and sky distribution of the clusters indicate that these objects are genuine young, intermediate and old open clusters within the Milky Way disk.

Compared to literature values, our final derived cluster parameters are presented in Table 4. We derived cluster reddening, extinction, distance, vertical component, and tangential velocity. Our derived extinctions range from A_{Ks} = 0.07 ± 0.03 to 0.57 ± 0.04 , colour excess from E(J - K_s) = 0.16 ± 0.03 to 0.60 ± 0.03 , distances from D = 2.19 ± 0.06 kpc to 8.94 ± 0.06 kpc,

and Galactocentric distances from R_G = 7.82 to 15.08 kpc. The Z component ranges from Z -0.09 to 0.34 kpc, and tangential velocities range from V_T = 30.59 to 245.42 km/s.

We also computed age and metallicity by fitting PARSEC isochrones, finding ages from t = 20 Myr to 5 Gyr and metallicity from [Fe/H] = -0.5 to 0.5 dex. Structural parameters were derived, with core radii ranging from r_c = 0.71 to 5.21', tidal radii from r_t = 3.6' to 12.0', and concentration indices from c = 0.36 to 0.83. These measurements confirm that the nine clusters examined are genuine young, intermediate and old open clusters. Finally, a spectroscopic follow-up is necessary to constrain the metallicity and chemical abundances of the clusters. Additionally, spectroscopic data will help determine the orbital parameters of each cluster.
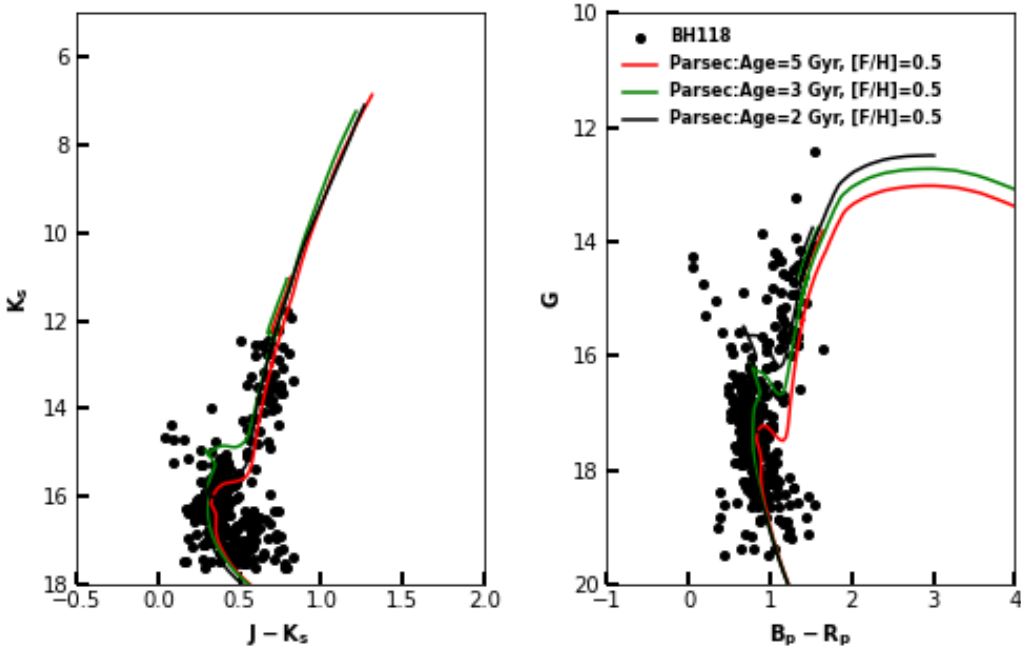
References

Abuter, R., Amorim, A., Bauböck, M., et al. 2019, A&A, 625, L10
Alonso-García, J., Minniti, D., Catelan, M., et al. 2017, ApJ, 849, L13
Alonso-García, J., Saito, R. K., Hempel, M., et al. 2018, A&A, 619, A4
Alves, D. R., Rejkuba, M., Minniti, D., & Cook, K. H. 2002, ApJ, 573, L51
Angelo, M., Santos, J., Corradi, W., & Maia, F. 2019, A&A, 624, A8
Ashman, K. M., Bird, C. M., & Zepf, S. E. 1994, AJ, 108, 2348
Babusiaux, C., Van Leeuwen, F., Barstow, M. A., et al. 2018, A&A, 616, A10
Bressan, A., Marigo, P., Girardi, L., et al. 2012, MNRAS, 427, 127
Buckner, A. S. & Froebrich, D. 2013, MNRAS, 436, 1465
Cantat-Gaudin, T., Anders, F., Castro-Ginard, A., et al. 2020, A&A, 640, A1
Cantat-Gaudin, T., Krone-Martins, A., Sedaghat, N., et al. 2019, A&A, 624, A126
Cardelli, J. A., Clayton, G. C., & Mathis, J. S. 1989, AJ, 345, 245
Carraro, G. & Chiosi, C. 1994, A&A, 287, 761
Castro-Ginard, A., Jordi, C., Luri, X., Cantat-Gaudin, T., & Balaguer-Núñez, L. 2019, A&A, 627, A35
Castro-Ginard, A., Jordi, C., Luri, X., et al. 2022, A&A, 661, A118
Castro-Ginard, A., Jordi, C., Luri, X., et al. 2018, A&A, 618, A59
Dias, W., Monteiro, H., Caetano, T., et al. 2014, A&A, 564, A79
Emerson, J. & Sutherland, W. 2010, The Messenger, 139, 2
Friel, E. 1995, ARA&A, 33, 381
Friel, E. D., Jacobson, H. R., & Pilachowski, C. A. 2010, AJ, 139, 1942
Frinchaboy, P. M., Majewski, S. R., Crane, J. D., et al. 2004, ApJ, 602, L21
Gaia-Collaboration et al. 2016, A&A, 595, A2
Gaia Collaboration, A. G., Vallenari, A., Prusti, T., et al. 2021, A&A, 649, A1
Garro, E., Minniti, D., Alessi, B., et al. 2022a, A&A, 659, A155
Garro, E., Minniti, D., Alonso-García, J., et al. 2024, arXiv preprint
Garro, E., Minniti, D., Gómez, M., et al. 2022b, A&A, 662, A95
González-Fernández, C., Hodgkin, S. T., Irwin, M. J., et al. 2018, MNRAS, 474, 5459
Hao, C., Xu, Y., Wu, Z., et al. 2022, A&A, 660, A4
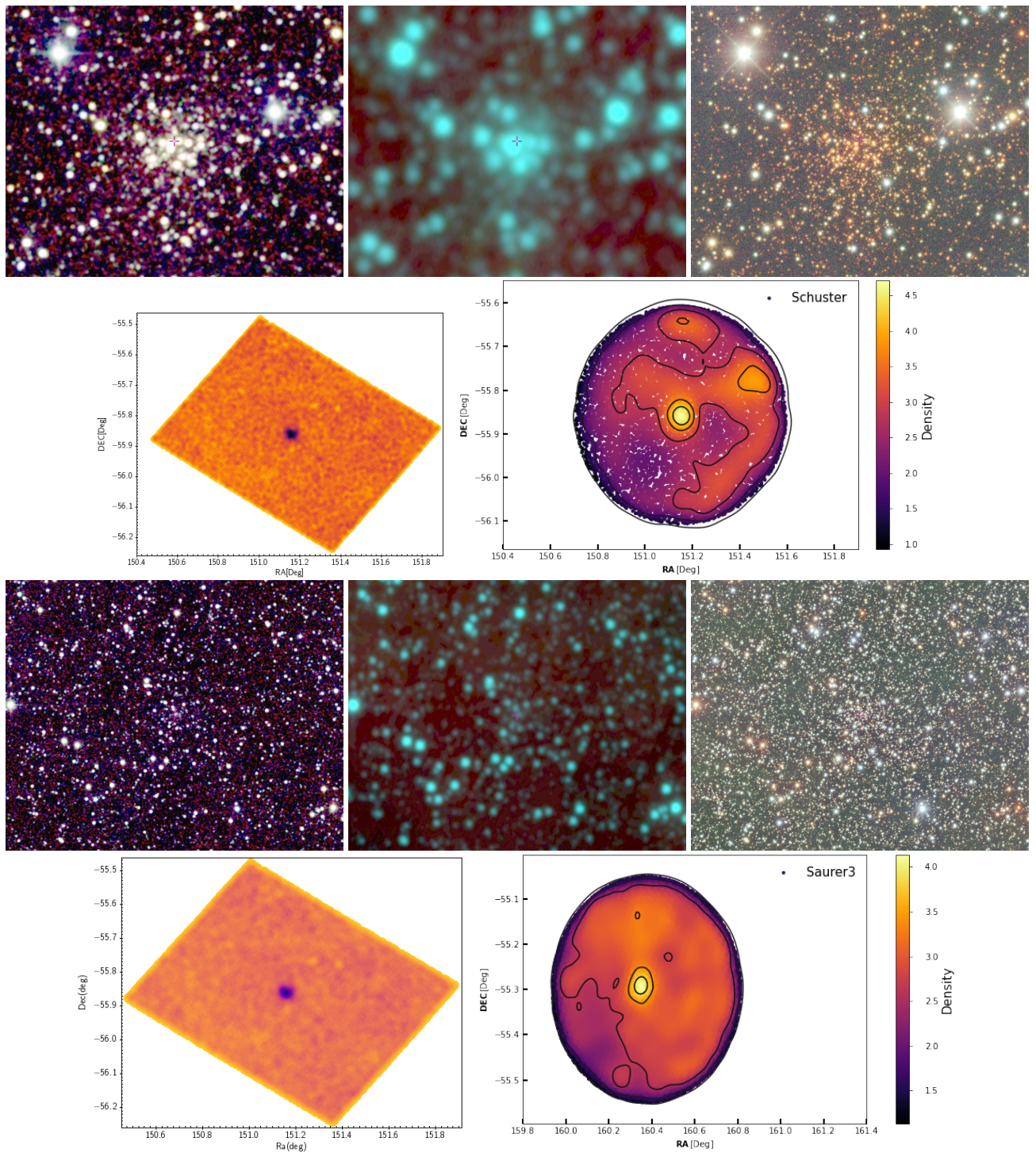Kharchenko, N., Piskunov, A., Schilbach, E., Röser, S., & Scholz, R.-D. 2013, A&A, 558, A53

Table 4. Derived physical parameters for each cluster compared with literature values from Cantat-Gaudin et al. (2020), Kharchenko et al. (2013), and Dias et al. (2014).

Name	$\mu_{\alpha*}$ [mas yr⁻¹]	μ_δ [mas yr⁻¹]	A_G	D_{Gaia}[kpc]	D_{avg} [kpc]	R_G [kpc]	Z [kpc]	E(B-V)	Age [Gyr]	r_c [pc]	r_t [pc]	c	$V_{T\alpha*}$ [km/s]	$V_{T\delta}$ [km/s]	V_T [km/s]	[Fe/H] [dex]
BH118	-5.493 ± 0.209	1.519 ± 0.280	1.39	7.10	8.34±0.03	9.29	0.34	0.53±0.05	3±0.5	1.78	11.89	0.83	−225.42	62.31	233.88	0.5
BH_144	-5.338 ± 0.095	-0.775 ± 0.780	2.16	6.60	8.81±0.10	7.82	-0.49	0.81±0.06	2±0.2	1.9	11.88	0.78	−242.76	−36.07	245.42	0.5
Schuster-MWSC1756	5.244 ± 0.199	3.167 ± 0.231	9.25	-	7.03±0.05	9.73	-0.03	3.47±0.20	700±0.2 Myrs	1.4	7.04	0.70	167.69	100.67	195.59	0.0
Saurer3	-5.043 ± 0.201	2.232 ± 0.909	2.20	8.70	7.23±0.04	9.41	0.38	0.83±0.06	2±0.2	1.6	9.6	0.77	−221.85	108.58	246.99	-0.5
FSR1521	-4.827 ± 0.050	3.317 ± 0.359	8.87	-	3.15±0.05	8.23	-0.09	3.33±0.20	1±0.2	2.5	8.9	0.55	−77.82	68.41	103.61	0.0
Saurer2	-2.362 ± 0.249	2.729 ± 0.342	5.02	-	5.49±0.05	10.77	-0.10	1.89±0.11	3±0.2	1.4	7.8	0.75	−71.17	95.14	118.82	0.0
Haffner10-FSR1231	-1.311 ± 0.941	1.436 ± 0.772	1.76	4.00	3.62±0.03	10.86	0.06	0.66±0.05	20±0.2 Myrs	1.2	6.8	0.74	−19.44	23.62	30.59	0.5
Juchert12	-0.872 ± 0.026	1.539 ± 0.051	2.23	8.70	8.94±0.06	15.08	-0.64	0.84±0.06	2±0.2	2.4	14.5	0.79	−30.72	66.34	73.11	-0.5
Pismis3	-4.755 ± 0.377	6.655 ± 0.011	3.75	1.10	2.19±0.06	8.92	0.02	1.41±0.09	3±0.2	3.18	7.3	0.36	−46.43	64.98	79.86	0.5
					Cantat-Gaudin et al. (2020) measurement											
BH118	-4.406	1.450	–	–	8.8	9.6	0.36	–	–	–	–	–	–	–	–	–
BH_144	-5.111	-0.375	–	–	9.6	8.3	-0.532	–	–	–	–	–	–	–	–	–
Schuster-MWSC1756	5.102	3.760	–	–	–	–	–	–	–	–	–	–	–	–	–	–
Saurer3	–	–	–	–	–	–	–	–	–	–	–	–	–	–	–	–
FSR1521	-4.886	4.467	–	–	4.933	8.886	-0.139	–	–	–	–	–	–	–	–	–
Saurer2	-2.969	4.567	–	–	6.4	–	-0.127	–	–	–	–	–	–	–	–	–
Haffner10-FSR1231	-1.144	1.557	–	–	3.4	10.8	0.06	–	–	–	–	–	–	–	–	–
Juchert12	–	–	–	–	–	–	–	–	–	–	–	–	–	–	–	–
Pismis3	-4.809	6.645	–	–	2.3	9.1	0.02	–	–	–	–	–	–	–	–	–
					Kharchenko et al. (2013) measurement											
BH118	–	–	–	–	–	–	–	–	–	–	–	–	–	–	–	–
BH_144	-13.19	7.74	–	–	7.2	–	–	0.63	1.0	0.83	12.88	–	–	–	–	-0.5
Schuster-MWSC1756	-9.41	3.06	–	–	1.8	–	–	1.08	6.3 Myrs	0.26	5.41	–	–	–	–	–
Saurer3	-8.34	4.40	–	–	7.1	–	–	0.78	1.9	9.18	20.46	–	–	–	–	–
FSR1521	-8.92	6.10	–	–	1.5	–	–	0.38	5.1 Myrs	0.84	6.69	–	–	–	–	–
Saurer2	-6.62	8.13	–	–	6.0	–	–	1.25	1.7	1.40	15.56	–	–	–	–	–
Haffner10-FSR1231	–	–	–	–	–	–	–	–	–	–	–	–	–	–	–	–
Juchert12	–	–	–	–	–	–	–	–	–	–	–	–	–	–	–	–
Pismis3	–	–	–	–	–	–	–	–	–	–	–	–	–	–	–	–
					Dias et al. (2014) measurement											
BH118	–	–	–	–	–	–	–	–	–	–	–	–	–	–	–	–
BH_144	-4.73	-3.36	–	–	–	–	–	–	–	–	–	–	–	–	–	–
Schuster-MWSC1756	–	–	–	–	–	–	–	–	–	–	–	–	–	–	–	–
Saurer3	-6.73	-1.62	–	–	–	–	–	–	–	–	–	–	–	–	–	–
FSR1521	–	–	–	–	–	–	–	–	–	–	–	–	–	–	–	–
Saurer2	–	–	–	–	–	–	–	–	–	–	–	–	–	–	–	–
Haffner10-FSR1231	-1.04	-0.36	–	–	–	–	–	–	–	–	–	–	–	–	–	–
Juchert12	-3.46	0.52	–	–	–	–	–	–	–	–	–	–	–	–	–	–
Pismis3	-3.42	3.82	–	–	–	–	–	–	–	–	–	–	–	–	–	–

Fig. 7. Colour-magnitude diagrams for BH118 cluster studied in both NIR and optical *Gaia* bands. These CMDs are fitted with Parsec isochrones to infer the age and [Fe/H] for each cluster.
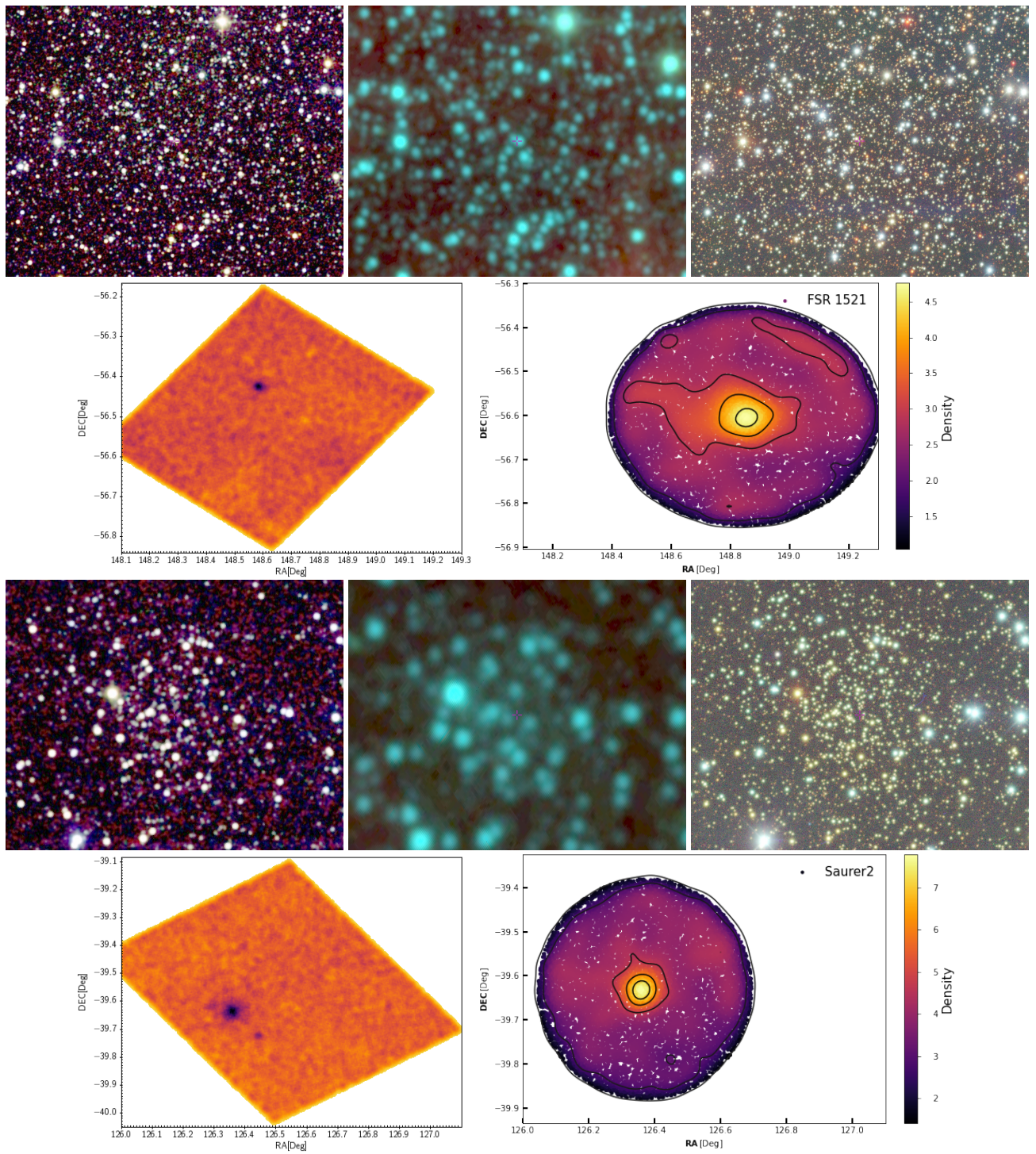
King, I. 1962, AJ, 67, 471
Kronberger, M., Teutsch, P., Alessi, B., et al. 2006, A&A, 447, 921
Marigo, P., Girardi, L., Bressan, A., et al. 2017, ApJ, 835, 77
Minniti, D., Lucas, P., Emerson, J., et al. 2010, New Astron, 15, 433
Montgomery, K. A., Janes, K. A., & Phelps, R. L. 1994, AJ, 108, 585
Muratov, A. L. & Gnedin, O. Y. 2010, AJ, 718, 1266
Nataf, D. M., Gonzalez, O. A., Casagrande, L., et al. 2015, MNRAS, 456, 2692

Nishiyama, S., Tamura, M., Hatano, H., et al. 2009, ApJ, 696, 1407
Obasi, C., Gomez, M., Minniti, D., & Alonso-Garcia, J. 2021, A&A, 654, A39
Obasi, C., Gomez, M., Minniti, D., et al. 2023, A&A, 670, A18
Obasi, C., Gómez, M., Minniti, D., et al. 2024, MNRAS, 529, 3075
Phelps, R. 1994, AJ, 107, 1079
Ruiz-Dern, L., Babusiaux, C., Arenou, F., Turon, C., & Lallement, R. 2018, A&A, 609, A116

Saito, R., Hempel, M., Alonso-García, J., et al. 2024, arXiv preprint
Saito, R. K., Hempel, M., Minniti, D., et al. 2012, A&A, 537, A107
Sanders, W. 1971, A&A, 14, 226
Saroon, S., Dias, B., Minniti, D., et al. 2024, A&A, 689, A115
Schlafly, E. F. & Finkbeiner, D. P. 2011, AJ, 737, 103
Schlegel, D. J., Finkbeiner, D. P., & Davis, M. 1998, ApJ, 500, 525
Siegert, T. 2019, A&A, 632, L1
Skrutskie, M., Cutri, R., Stiening, R., et al. 2006, AJ, 131, 1163
Stetson, P. B. 1980, AJ, 85, 387
Tarricq, Y., Soubiran, C., Casamiquela, L., et al. 2022, A&A, 659, A59
Taylor, M. B. 2005, in Astronomical data analysis software and systems XIV,
    Vol. 347, 29
Tosi, M., Bragaglia, A., & Cignoni, M. 2007, MNRAS, 378, 730
Tosi, M., Pulone, L., Marconi, G., & Bragaglia, A. 1998, MNRAS, 299, 834
Vasilevskis, S., Klemola, A., & Preston, G. 1958, AJ, 63, 387
York, D. G., Adelman, J., Anderson Jr, J. E., et al. 2000, AJ, 120, 1579
Zhao, J. & He, Y. 1990, A&A, 237, 54
Zhao, J. & Shao, Z. 1994, A&A, 288, 89
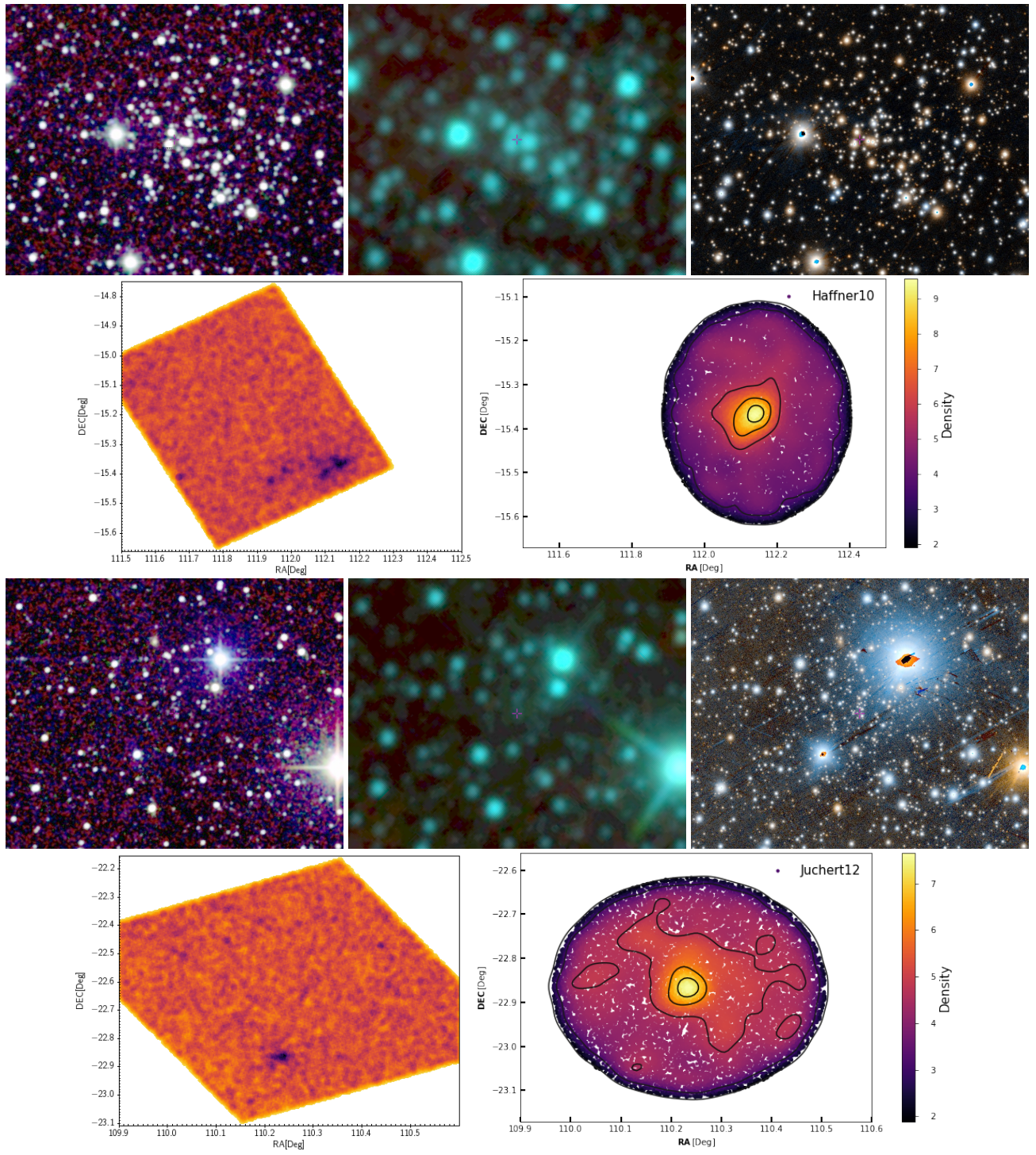
Fig. A.1. Same as Fig. 2, but for the clusters Schuster and Sauer 3.
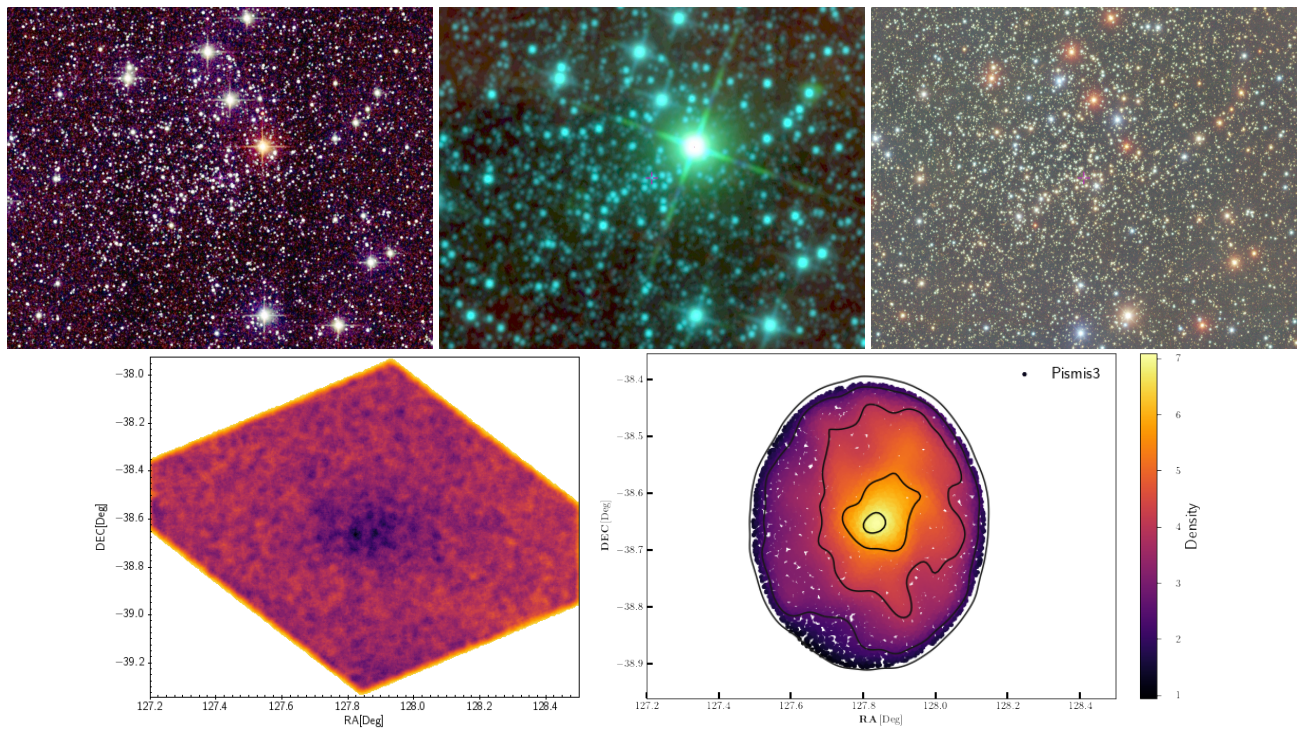
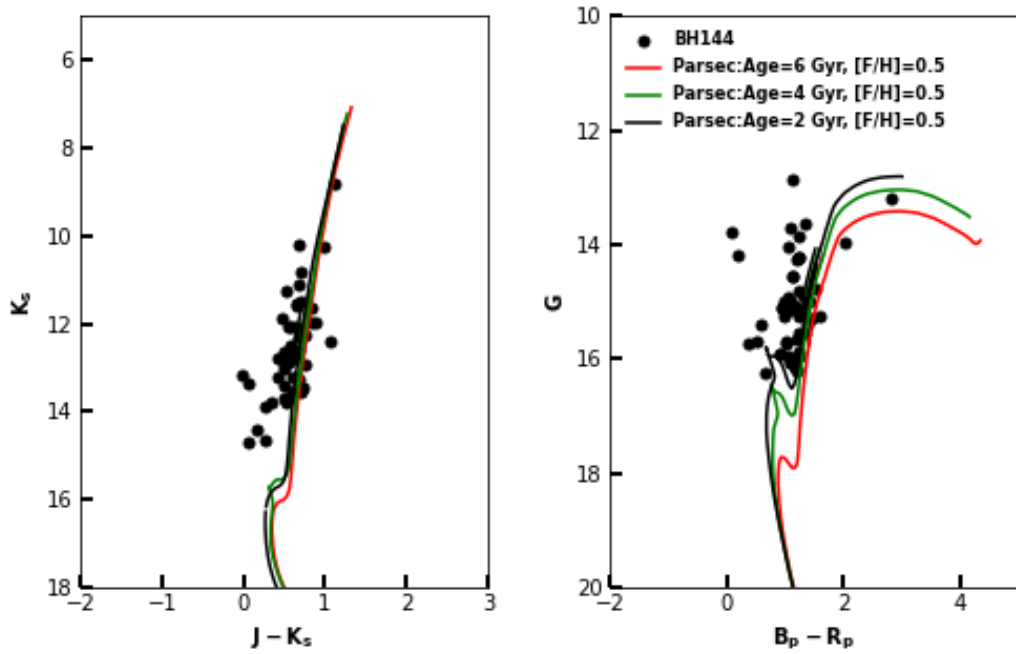## Appendix A: Additional figures

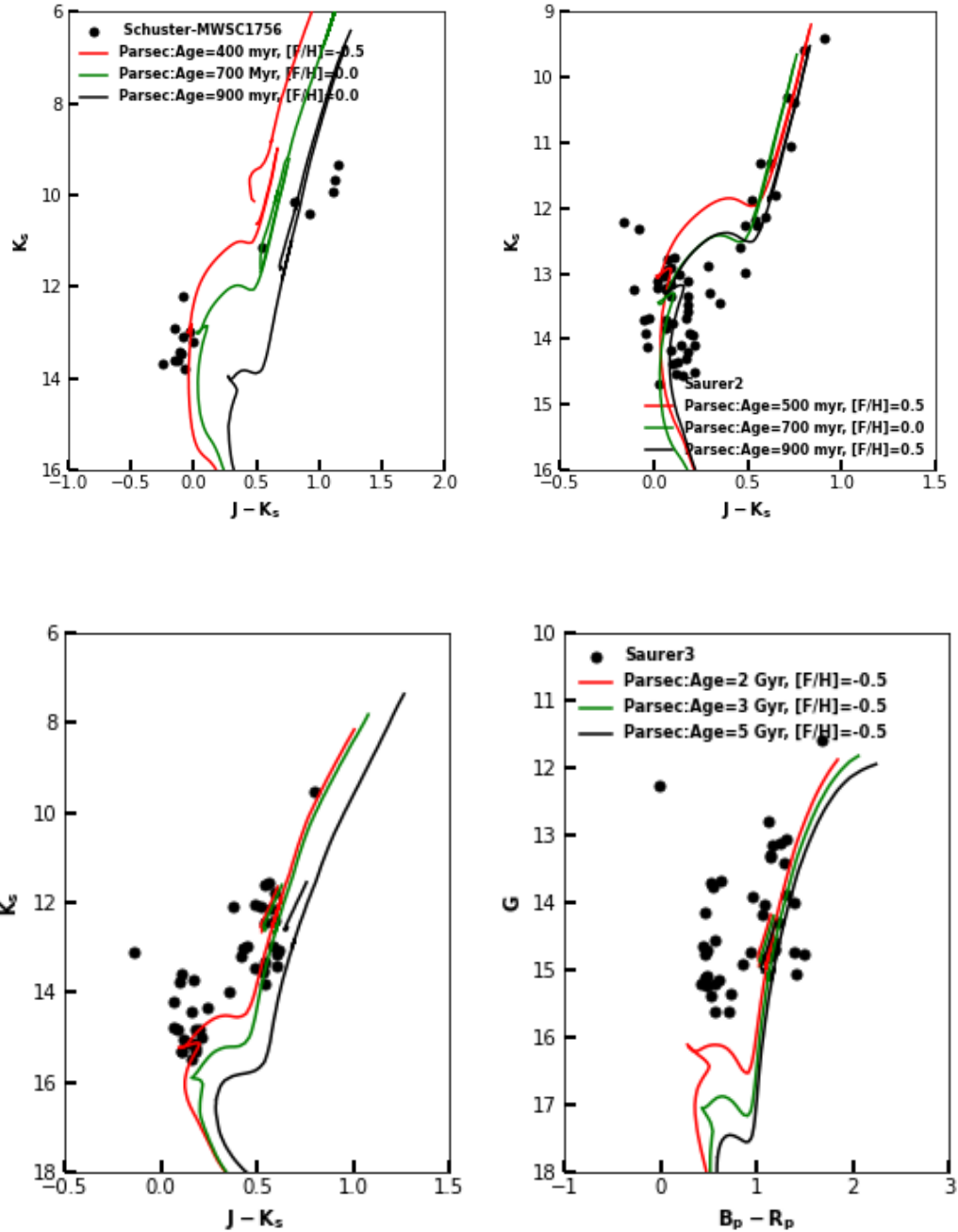**Fig. A.2.** Same as Fig. 2, but for the clusters FSR 1521 and Sauer 2.

Fig. A.3. Same as Fig. 2, but for the clusters Haffner10 and Juchert 12, however, the right image in the first and third panels is from Pan-STARRS.
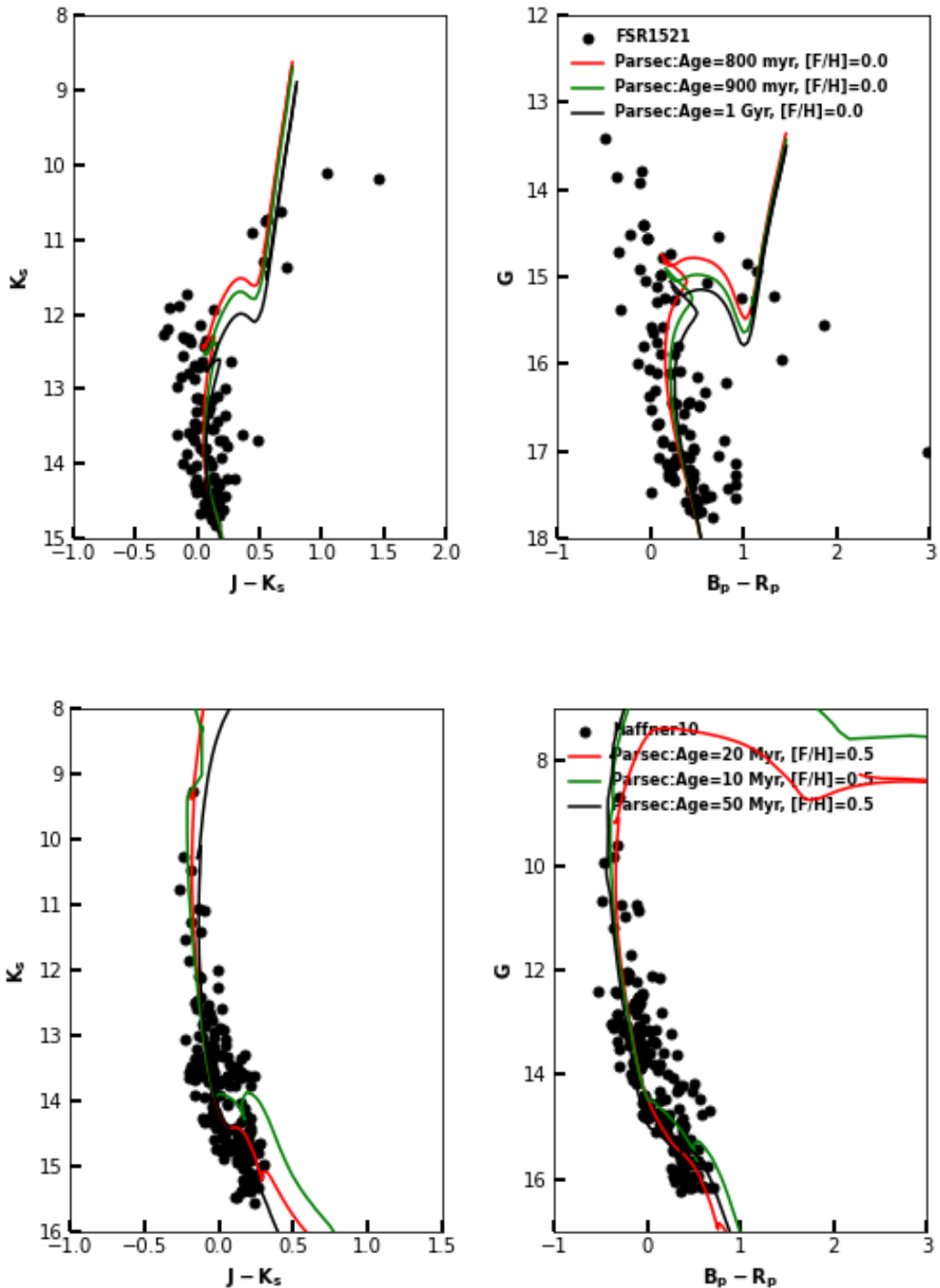
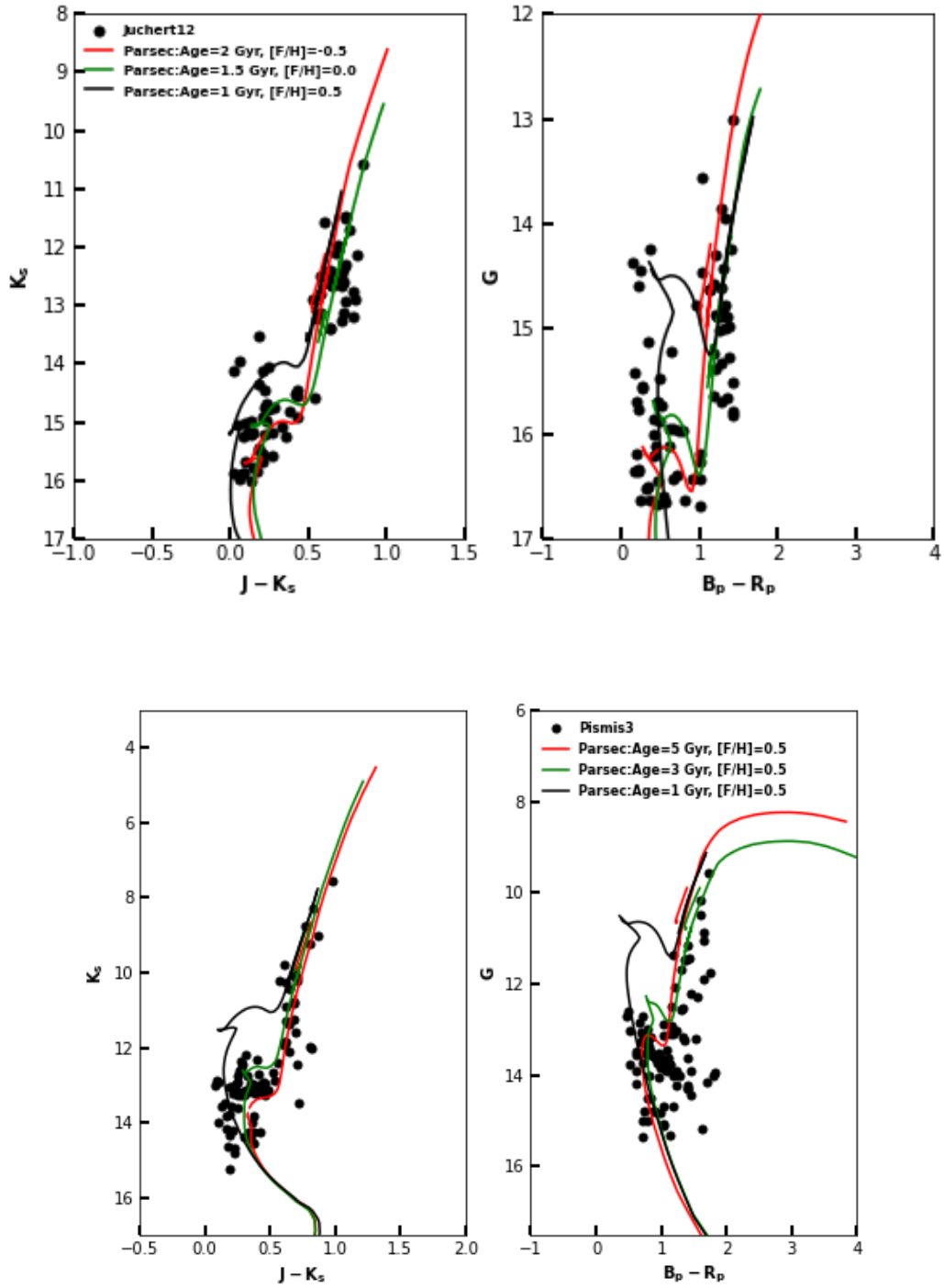**Fig. A.4.** Same as Fig. 2, but for the cluster Pismis3.

Fig. A.5. Colour-magnitude diagrams fo BH144 cluster studied in both NIR and optical *Gaia* bands. These CMDs are fitted with Parsec isochrones to infer the age and [Fe/H] for each cluster.
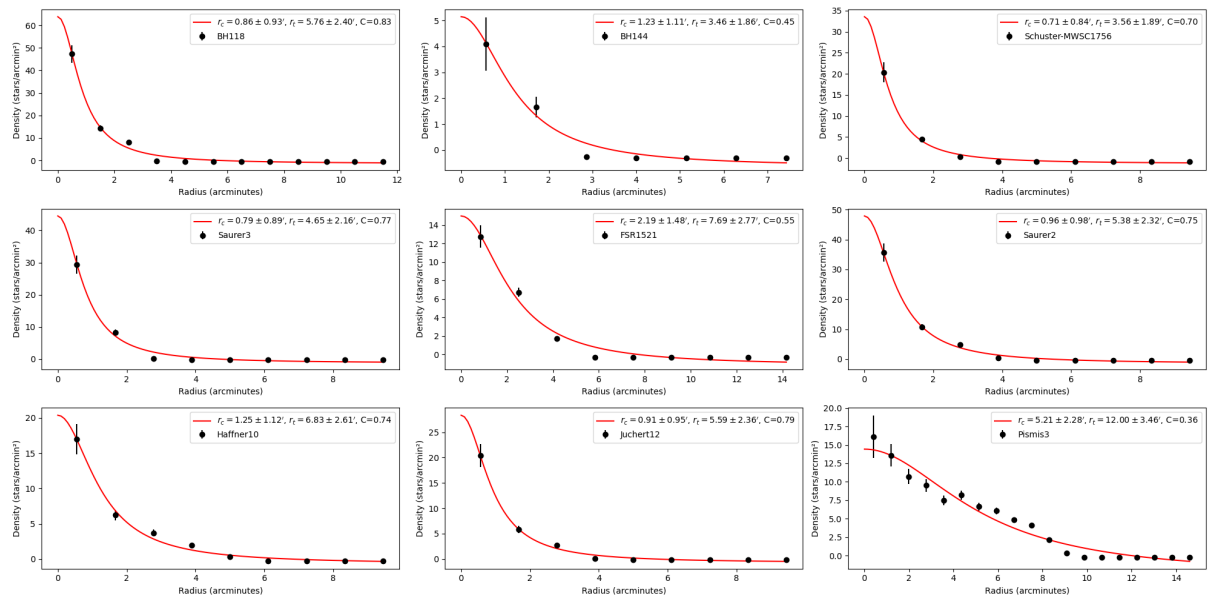
Fig. A.6. Same as Figure 11 but for Schuster, Saurer2 (upper-left and upper-right panels), and Saurer 3 (bottom panel). For clusters with high optical extinction $A_G > 4$, CMDs are not presented.

Fig. A.7. Same as Figure 11 but for FSR1521 and Haffner10. For FSR1521, despite the extinction value $A_V > 4$, the Gaia CMD is well populated in the main sequence, distinguishing it from other CMDs with similar extinction values. Consequently, we calculated the distance modulus using the distance measured from parallax.

Fig. A.8. Same as Figure 11 but for Juchert12 and Pismis3.

Fig. A.9. The radial density profile of the clusters is presented, with black points representing the number of stars per unit area within an annular bin. The red line indicates the best-fit King model profile (King 1962).